International Journal of Solids and Structures 229 (2021) 111148

Contents lists available at ScienceDirect

International Journal of Solids and Structures

journal homepage: www.elsevier.com/locate/ijsolstr

Limit load instabilities of anisotropic tubes under combined tension and torsion

Kelin Chen [a,b], Stelios Kyriakides [a,*]

[a] Research Center for Mechanics of Solids, Structures & Materials, ASE, 2617 Wichita St, The University of Texas at Austin, Austin, TX 78712, United States
[b] Department of Integrated Systems Engineering, The Ohio State University, 210 Baker Systems, Columbus, OH 43210, United States

ARTICLE INFO

Article history:
Received 4 November 2020
Received in revised form 6 February 2021
Accepted 25 June 2021
Available online 1 July 2021

Keywords:
Limit load instability
Combined tension and torsion
Anisotropy
Material hardening
Material frame rotation

ABSTRACT

Under tensile loadings, thin-walled structures such as sheet metal and tubes develop load maxima, or limit loads, beyond which deformation localizes leading to rupture. For uniform stress states, Considère-type estimates of limit loads can serve as forming limits in applications. The paper explores the effect of anisotropy on such estimates for thin-walled Al-alloy tubes under combined tension and torsion. Anisotropy is modeled using Yld04-3D with an exponent of 8. Material hardening originates from a simple shear test using this yield function, taking into account material axes rotation caused by the shearing. A Considère formulation is developed for the problem, which also incorporates the effect of material frame rotation. The analysis is used to establish limit loads for a set of circumferentially constrained tension–torsion experiments tested under radial nominal tension-shear stress paths. The predictions reproduce the strains measured at the limit loads for the range of biaxiality ratios considered. By contrast, corresponding results produced using the isotropic yield functions of von Mises and Hosford(8) increasingly deviate from the measured results as the shear stress increases. Considère-type formulation is also developed for the same tension–torsion loadings for a uniform thickness tube. The results exhibit a similar trend but the limit strains for shear dominant paths are significantly lower, demonstrating the stabilizing effect of the circumferential constraint used in the experiments.

1. Introduction

The response of thin-walled structures made of ductile metals to tensile loads is typically characterized by a load maximum or *limit load*. Beyond this point deformation localizes leading to rupture. Consequently, the strains associated with a limit load represent a forming limit for the structure. For example, such limit states develop in thin-walled sheets under biaxial loads encountered in forming processes, and thin-walled tubes under combined internal pressure, tension and torsion. The classical Considère (1885) condition for the limit load of bars under tension is also applicable to biaxial stress states, and can provide an analytical alternative to numerical solutions for establishing such critical states. The tensile instability of thin-walled sheets and tubes was investigated by Swift (1952), Mellor (1962), Hillier (1963), Stout & Hecker (1983), Section 5 of Butcher and Abedini (2019) among others, and is rather well established. More recently plastic anisotropy has been shown to also influence tensile instabilities of thin-walled structures (e.g., Scales et al., 2021, for combined tension and pressure, see also Hillier (1974) for a tube under internal pressure).

In our recent study of the response and failure of thin-walled tubes under combined shear and tension – Scales et al. (2019), Chen et al. (2019) – we encountered a challenge to such calculations brought about by plastic anisotropy. Aluminum 6061-T6 tubes were tested to failure under a set of stress paths in the nominal axial-shear stress space

$$\Sigma = \alpha \mathcal{T}, \cdots 0 \leqslant \alpha \leqslant 4. \tag{1}$$

For $\alpha < 3.5$, the machine is operated in rotation and axial load control, with the torque acting as the command signal for the force. For $\alpha \geqslant 3.5$ the machine is operated in axial displacement and torque control, with the force acting as the command signal for the torque. With the exception of the pure torsion test ($\alpha = 0$), the nominal axial and shear stress responses recorded developed limit loads, beyond which deformation localized into narrow circumferential bands which subsequently ruptured (see Fig. 10 in Scales et al., 2019). The material exhibited plastic anisotropy, which was modeled using the Yld04-3D anisotropic yield function (Barlat et al., 2005) calibrated in Appendix A of Chen et al. (2019).

* Corresponding author.
E-mail address: skk@mail.utexas.edu (S. Kyriakides).

https://doi.org/10.1016/j.ijsolstr.2021.111148
0020-7683/

The hardening response of the material was established from a pure torsion test on a thin-walled tube using the Yld04-3D model as well as the isotropic von Mises and the non-quadratic Hosford (1972) yield functions. Chen et al. (2018) pointed out that shear rotates the material axes and the rotation must be accounted for when the material exhibits plastic anisotropy (see also Abedini et al., 2020). A way of accounting for the material frame rotation is outlined in this reference where it was applied to the Hill-48 (H-48, Hill, 1948) quadratic anisotropic yield function. Subsequently Chen et al. (2019) incorporated material frame rotation in the calibration of Yld04-3D. The extracted plastic equivalent stress–strain response for H-48 and Yld04-3D, referred to as *Material Frame* (MF), are plotted in Fig. 1. Included in the figure are the hardening responses corresponding to the von Mises (vM) and Hosford (H8) yield functions. The four hardening responses differ from each other pointing to the need that each be used with the corresponding yield function in analyses (see Tardif & Kyriakides, 2012).

These calculations showed that for anisotropic yield functions material frame rotation affects the equivalent stress and strain. Since Considère limit load estimates for uniform stress-states depend on the equivalent stress and strain, frame rotation must be accounted for when such estimates are based on anisotropic yield functions. The paper uses the Yld04-3D and H-48 anisotropic yield functions to examine the effect of frame rotation on the prediction of the limit strain under combined tension and shear. The limit strains predicted by the analytic expressions developed are evaluated by comparing them with results from finite element calculations and the values measured in the tension–torsion experiments of Scales et al. (2019). The experiments considered were performed on tubes with a relatively short, thin-walled test section. This setting constrains hoop deformation and stabilizes the structure. To highlight this stabilizing effect, we also analyze a tube with uniform thickness under combined tension and torsion.

2. Analysis

2.1. The problem

The tension–torsion experiments of Scales et al. (2019) involved thick-walled Al-6061-T6 tubes (1.969 × 0.173 in – 50 × 4.38 mm) into which a thin-walled test section was machined as shown in Fig. 2 with the following geometry: {height, L_g, mean radius, R, thickness, t_o} = {0.400, 0.833, 0.039} in – {10.2, 21.2, 1.00} mm and $R/t_o \approx 21.4$. The experiments were simulated via finite element analysis using the Yld04-3D, vM and H8 constitutive models in Chen et al. (2019). Fig. 3 compares predictions from the three constitutive models against the measured nominal shear stress-rotation ($\mathcal{T} - \phi$) and axial stress-elongation ($\Sigma - \delta/L_g$) responses for stress ratio $\alpha = 0.75$ (ϕ and δ are respectively the rotation and the elongation of the test section shown in Fig. 2). Marked on each response with triangular symbols is the limit load. The Yld04-3D and H8 responses follow the experimental results well developing some difference after the limit load. The vM responses on the other hand trace lower stress trajectories with the shear limit stress occurring at significantly smaller rotation angle. Fig. 4 plots the equivalent plastic strain (ε_e^p) at the most deformed point in the test section against the twist angle. Initially the strain grows nearly linearly with ϕ for all cases. As the limit load is approached, growth accelerates and beyond it becomes increasingly more rapid within the localizing band. The trajectories predicted using H8 and Yld04-3D track the experimental one well. The vM analysis developed a limit load much earlier and consequently the localization occurs at much smaller ϕ. Collectively the results of Chen et al. (2019) demonstrated that for Al-alloys, accurate prediction of the inelastic response and large deformation behavior associated with localized deformation requires the adoption of a non-quadratic yield function and accurate representation of the anisotropy. At the same time, the results demonstrate the importance of the limit load strain in design.

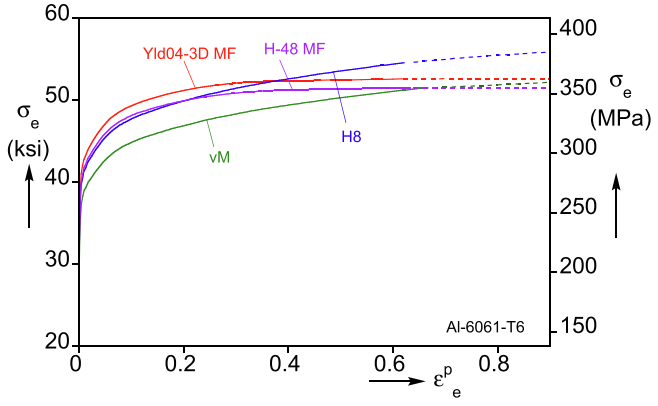

Fig. 1. Equivalent stress–strain responses extracted from a pure torsion experiment on an Al-6061-T6 tube using the isotropic vM and H8 and the anisotropic Yld04-3D and H-48 constitutive models. The anisotropic models account for material frame rotation.

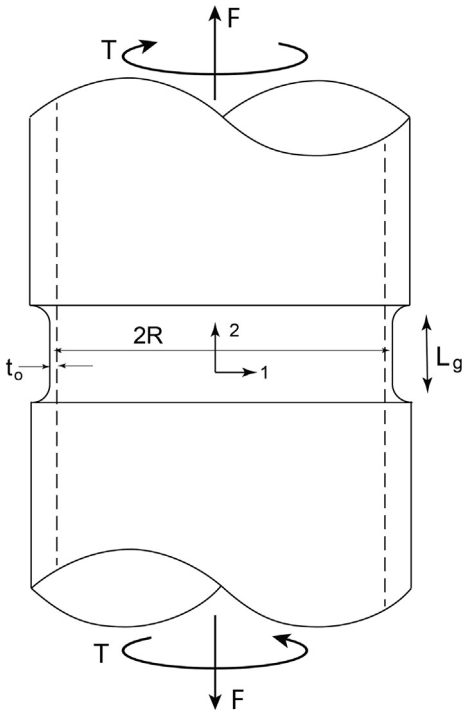

Fig. 2. Schematic of the geometry of the test specimen used in the tension–torsion experiments of Scales et al. (2019). The test section is essentially circumferentially constrained.

For the set-up in Fig. 2, let the test section radius be R and its wall-thickness $t_o << R$. Designate x_1, x_2 and x_3 as the hoop, axial, and radial direction coordinates. The Cauchy hoop, axial, and shear stresses are $\{\sigma_{11}, \sigma_{22}, \sigma_{12}\}$ while the through thickness stress σ_{33} is negligibly small. Let the corresponding logarithmic strains be ε_{ij}. Since the specimens were loaded along radial paths in the nominal axial-shear stress space, $\Sigma = \alpha\mathcal{T}$, the corresponding true stresses are

$$\sigma_{22} = \alpha\sigma_{12}e^{\varepsilon_{11}} \tag{2a}$$

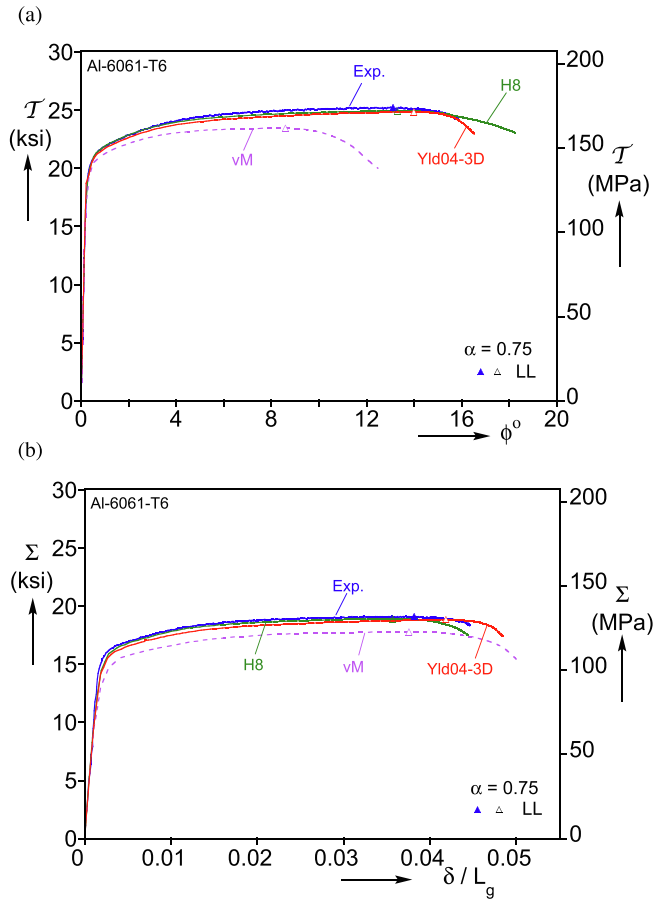

Fig. 3. Comparison of measured and predicted responses using three different constitutive models for $\alpha = 0.75$ from Chen et al. (2019). (a) Nominal shear stress-rotation and (b) nominal axial stress-elongation (ϕ and δ are the rotation and elongation of the test section).

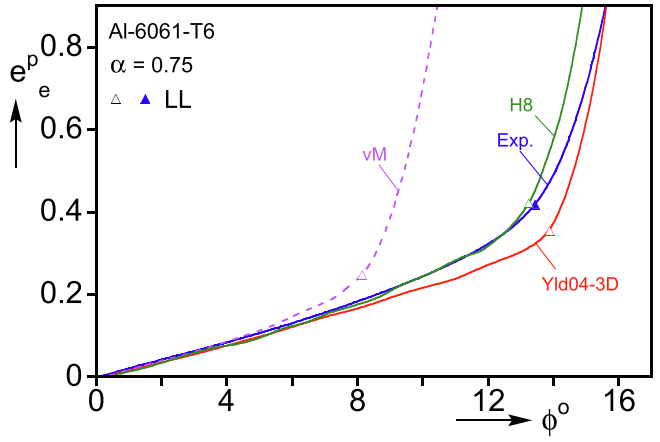

Fig. 4. Measured equivalent plastic strain in the localizing zone vs. rotation for $\alpha = 0.75$, and corresponding ones calculated using the vM, H8 and Yld04-3D constitutive models.

(for the importance of the control variables on the limit load see Hill, 1996). The circumferential constraint of the text section implies that

$$d\varepsilon_{11} = 0 \text{ and } \sigma_{11} = \beta\sigma_{22}. \tag{2b}$$

The principal stresses are then

$$\sigma_{1,2} = \frac{\sigma_{22}}{2}\left[(1+\beta) \pm \sqrt{(1-\beta)^2 + 4/\alpha^2}\right]. \tag{2c}$$

Chen et al. (2019) simulated the tension-torsion experiments using a finite element model together with the von Mises yield function (vM), the non-quadratic yield function of Hosford (1972) with exponent of 8 (H8), and the non-quadratic anisotropic three-dimensional yield function of Barlat et al. (2005) Yld04-3D with the same exponent. The same yield functions are adopted here. For the stress state of the present problem, vM reduces to:

$$\Phi = [\sigma_{11}^2 - \sigma_{11}\sigma_{22} + \sigma_{22}^2 + 3\sigma_{12}^2]^{1/2}. \tag{3}$$

H8 expressed in terms of the principal stresses is

$$\Phi = \{[(\sigma_1 - \sigma_2)^8 + \sigma_2^8 + \sigma_1^8]/2\}^{1/8} \tag{4}$$

The Yld04-3D can be written as

$$\begin{aligned}\Phi = \; & [(|S'_1 - S''_1|^8 + |S'_1 - S''_2|^8 + |S'_1 - S''_3|^8 + |S'_2 - S''_1|^8 + |S'_2 - S''_2|^8 \\ + \; & |S'_2 - S''_3|^8 + |S'_3 - S''_1|^8 + |S'_3 - S''_2|^8 + |S'_3 - S''_3|^8])/4]^{1/8}\end{aligned} \tag{5}$$

where $\boldsymbol{S}'$ and $\boldsymbol{S}''$ are linear transformations of the Cauchy stress tensor through which orthotropic anisotropy is introduced. The transformations introduce 18 anisotropy parameters (see Barlat et al., 2005), which were evaluated as described in Appendix A of Chen et al. (2019) and are listed in Table 1.

2.2. Limit load for a general yield function

The limit load instability is the result of wall thinning of the test section caused by the axial force, F. Let the tube be finitely deformed to a current radius and thickness $\{r, t\}$, and assume the elastic strains to be negligibly small. At the load maximum

$$dF = 0 \;\Rightarrow\; \frac{d\sigma_{22}}{\sigma_{22}} + \frac{dt}{t} + \frac{dr}{r} = 0$$

$$or \; \frac{d\sigma_{22}}{\sigma_{22}} + d\varepsilon_{33} + d\varepsilon_{11} = 0 \tag{6a}$$

Using incompressibility in (6a) leads to

$$d\sigma_{22} = \sigma_{22} d\varepsilon_{22}. \tag{6b}$$

Proportionality between the axial force and the torque, T, implies also that

$$dT = 0 \Rightarrow \frac{d\sigma_{12}}{\sigma_{12}} + \frac{dt}{t} + 2\frac{dr}{r} = 0 \tag{7a}$$

Using incompressibility together with $d\varepsilon_{11} = 0$ leads to:

$$d\sigma_{12} = \sigma_{12} d\varepsilon_{22} \tag{7b}$$

Let Φ be the yield function and $\sigma_e(\sigma_{11}, \sigma_{22}, \sigma_{12}, \psi)$ the associated equivalent stress, where ψ is the rotation of the material frame (see Fig. A1). Then,

$$\begin{aligned} d\sigma_e &= \frac{\partial \Phi}{\partial \sigma_{11}} d\sigma_{11} + \frac{\partial \Phi}{\partial \sigma_{22}} d\sigma_{22} + \frac{\partial \Phi}{\partial \sigma_{12}} d\sigma_{12} + \frac{\partial \Phi}{\partial \psi} d\psi \\ &= \left(\frac{\partial \Phi}{\partial \sigma_{22}} + \frac{\sigma_{12}}{\sigma_{22}}\frac{\partial \Phi}{\partial \sigma_{12}} + \frac{\partial \Phi}{\partial \psi}\frac{d\psi}{d\sigma_{22}}\right)\sigma_{22} d\varepsilon_{22}. \end{aligned} \tag{8}$$

Plastic work compatibility requires

$$\sigma_e d\varepsilon_e = \sigma_{22} d\varepsilon_{22} + 2\sigma_{12} d\varepsilon_{12} = \sigma_{22} d\varepsilon_{22}\left(1 + \frac{2\sigma_{12}}{\sigma_{22}}\frac{d\varepsilon_{12}}{d\varepsilon_{22}}\right). \tag{9}$$

(In these calculations elastic strains are neglected so the equivalent plastic strain increment is depicted by $d\varepsilon_e$.) Furthermore, from (6b) and adopting $d\psi = -d\varepsilon_{12}$ from Appendix A

Table 1
Anisotropy parameters for Yld04-3D model.

c'_{12}	c'_{13}	c'_{21}	c'_{23}	c'_{31}	c'_{32}	c'_{44}	c'_{55}	c'_{66}
1.028	1.150	1.162	0.941	0.679	0.985	1.0	1.0	1.367
c''_{12}	c''_{13}	c''_{21}	c''_{23}	c''_{31}	c''_{32}	c''_{44}	c''_{55}	c''_{66}
0.713	0.683	0.847	1.093	1.056	0.962	1.0	1.0	0.695

$$\frac{d\psi}{d\sigma_{22}} = \frac{1}{\sigma_{22}}\frac{d\psi}{d\varepsilon_{22}} = -\frac{1}{\sigma_{22}}\frac{d\varepsilon_{12}}{d\varepsilon_{22}} \tag{10}$$

Combining (8) and (9) and adopting (10) leads to

$$\frac{d\sigma_e}{d\varepsilon_e} = \sigma_e \frac{\left(\frac{\partial \Phi}{\partial \sigma_{22}} + \frac{\sigma_{12}}{\sigma_{22}}\frac{\partial \Phi}{\partial \sigma_{12}} - \frac{1}{\sigma_{22}}\frac{\partial \Phi}{\partial \psi}\frac{d\varepsilon_{12}}{d\varepsilon_{22}}\right)}{\left(1 + \frac{2\sigma_{12}}{\sigma_{22}}\frac{d\varepsilon_{12}}{d\varepsilon_{22}}\right)}. \tag{11}$$

$$\text{Using the flow rule, } \frac{d\varepsilon_{12}}{d\varepsilon_{22}} = \frac{1}{2}\frac{\partial \Phi/\partial \sigma_{12}}{\partial \Phi/\partial \sigma_{22}}. \tag{12}$$

(Note that (12) can be obtained from the material frame application of the flow rule by a standard transformation of the strains and stresses.) Furthermore, applying the circumferential constraint, $\varepsilon_{11} = 0$, to (2a) leads to: $\sigma_{22} = \alpha\sigma_{12}$ and thus (11) becomes

$$\frac{d\sigma_e}{d\varepsilon_e} = \sigma_e \left[\frac{\partial \Phi}{\partial \sigma_{22}} - \frac{\frac{1}{2\sigma_{22}}\frac{\partial \Phi}{\partial \psi}\frac{\partial \Phi}{\partial \sigma_{12}}}{\frac{\partial \Phi}{\partial \sigma_{22}} + \frac{1}{\alpha}\frac{\partial \Phi}{\partial \sigma_{12}}}\right]. \tag{13}$$

It is worth noting that the derivatives of Φ in (13) are functions of (α, β, ψ) and the relationships between the three must be evaluated numerically as described in the next section. For the isotopic yield functions (13) reduces to:

$$\frac{d\sigma_e}{d\varepsilon_e} = \sigma_e \frac{\partial \Phi}{\partial \sigma_{22}}. \tag{14}$$

2.3. Limit load solution

a. Relationships between the problem variables (α, β, ψ) can be obtained from the constraint $d\varepsilon_{11} = 0$, which implies that $\frac{\partial \Phi}{\partial \sigma_{11}}(\alpha, \beta, \psi) = 0$. This can be solved numerically for fixed values of α producing $\psi - \beta$ relationships like the ones in Fig. 5a.
b. Work compatibility (9) can be written as

$$\begin{aligned} &\sigma_e d\varepsilon_e = \sigma_{22}\frac{d\varepsilon_{22}}{d\varepsilon_{12}}\left(1 + \frac{2}{\alpha}\frac{d\varepsilon_{12}}{d\varepsilon_{22}}\right)d\varepsilon_{12}, \\ &\text{or } d\varepsilon_e = -\frac{2\sigma_{22}}{\sigma_e}\left(\frac{\partial \Phi/\partial \sigma_{22}}{\partial \Phi/\partial \sigma_{12}} + \frac{1}{\alpha}\right)d\psi. \end{aligned} \tag{15}$$

Since the ratio of $\sigma_{22}/\sigma_e = f(\alpha, \beta, \psi)$, use the $\psi - \beta$ relationship generated for chosen values of α to make the RHS of (15) strictly a function of ψ. Integration produces $\varepsilon_e - \psi$ relationships like the ones in Fig. 5b.

c. The limit load for a chosen stress ratio can then be evaluated from the Considère condition (13) as follows. Select a value of ε_e and evaluate the corresponding σ_e and the local tangent modulus $d\sigma_e/d\varepsilon_e$ from the material hardening response (Fig. 1). Obtain the corresponding ψ from the $\varepsilon_e - \psi$ relationship. Evaluate the derivatives of Φ using the corresponding values of ψ and β, and compare the RHS of (13) with the value on the LHS. If they do not agree, increase ε_e and repeat until they do, which gives the equivalent strain at the limit load.

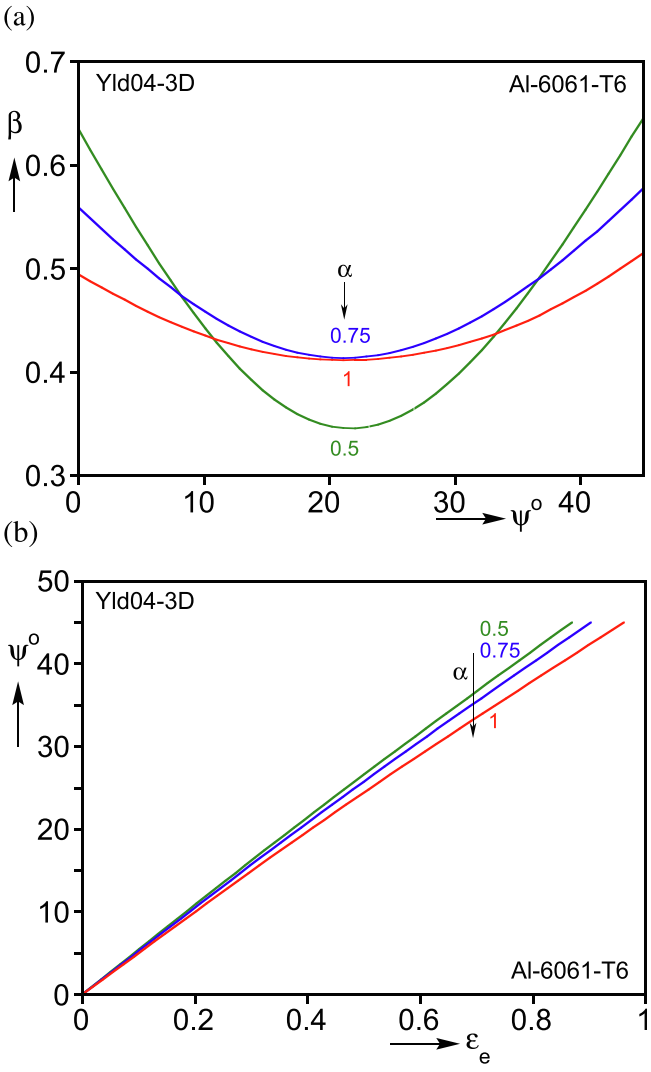

Fig. 5. (a) Stress ratio $\beta = \sigma_{11}/\sigma_{22}$ vs. the material rotation angle ψ for three values of α. (b) Equivalent strain vs. ψ for the same values of α.

2.4. Limit loads for isotropic yield functions

2.4.1. Von Mises

For the circumferentially constrained case $(d\varepsilon_{11} = 0)$, the von Mises yield function implies that $\beta = 1/2$ and the Considère condition (14) becomes

$$\frac{d\sigma_e}{d\varepsilon_e} = \frac{\sqrt{3}\sigma_e}{2[1 + 4/\alpha^2]^{1/2}}. \tag{16}$$

2.4.2. Hosford(8)

For the circumferentially constrained case β varies with α. The relationship is derived in Appendix B and plotted in Fig. B1. The Considère condition (14) becomes

$$\frac{d\sigma_e}{d\varepsilon_e}=\frac{\sigma_e}{2^{9/8}[1+\Gamma^8+(1-\Gamma)^8]^{7/8}}\left[1+\Gamma^7+\frac{(1-\beta)[1+2(1-\Gamma)^7-\Gamma^7]}{[(1-\beta)^2+4/\alpha^2]^{1/2}}\right] \tag{17a}$$

$$\text{where } \Gamma=\frac{\sigma_2}{\sigma_1}=\frac{1+\beta-[(1-\beta)^2+4/\alpha^2]^{1/2}}{1+\beta+[(1-\beta)^2+4/\alpha^2]^{1/2}} \tag{17b}$$

3. Results

Expression (13) and the numerical procedure of Section 2.3 are now used to evaluate the plastic equivalent strain corresponding to the limit load, ε_{eL}, for different stress ratios, α. The strains are plotted in Fig. 6 against $\tan^{-1}\alpha$ for better clarity. Drawn with a solid line are the results for the Yld04-3D anisotropic yield function used in conjunction with the corresponding material hardening response in Fig. 1. The tension–torsion tests were also simulated numerically using a finite element model and solution procedure

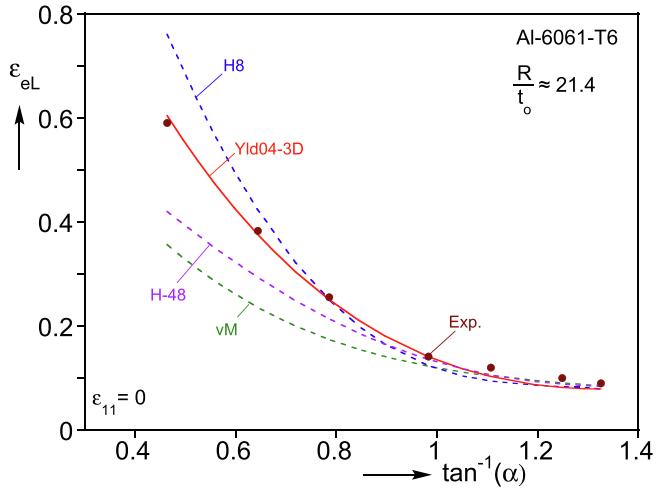

Fig. 6. Predicted equivalent strains at the limit loads vs. the stress ratio α. Included are predictions for Yld04-3D, H-48, vM and H8 constitutive models.

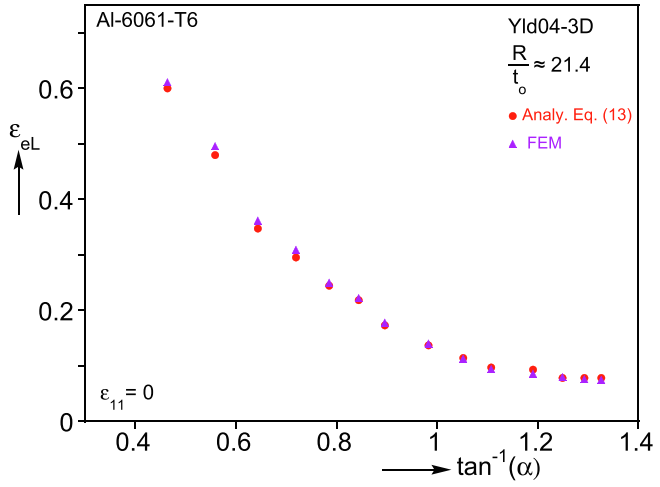

Fig. 7. Comparison of limit load equivalent strains calculated with the present analysis and by a finite element model over the range of α of interest.

along the lines of those described in Section 3.1 of Chen et al. (2019). Since here interest is limited to establishing the limit load, we opted to use an axisymmetric FE model, which makes the simulation much less computationally intensive. Fig. 7 compares the values of ε_{eL} evaluated through the FE analysis and those produced through Eq. (13) for stress ratios in the range of $0.5 \leqslant \alpha \leqslant 4.0$. The two sets of results are very close to each other for the whole range of α, thus confirming the accuracy of the analytical limit load solution.

The Yld04-3D analytic results are also compared to the limit strains corresponding to the seven experiments of Scales et al. (2019) in Fig. 6. The experimental data are seen to be in generally very good agreement with the analytic results thus providing one more confirmation of the veracity of the analysis. Included in the figure are predictions of limit load equivalent strains for vM and H8. Both track the Yld04-3D predictions well for stress ratios larger than 2. However, vM produces progressively lower strains as α is reduced from 2 to 0.5. For the 0.5 stress ratio the vM value is only 58% of the Yld04-3D result. This level of poor performance confirms once more that an isotropic quadratic representation of the yield function is not appropriate for Al-alloys. By contrast, the isotropic H8 predictions remain close to the anisotropic results up to a stress ratio of 1.0, but overestimate them for lower values of α. This points to the importance of anisotropy to the problem.

For comparison, we also considered the Hill-48 anisotropic quadratic yield function (Hill, 1948 – H-48), which for the present problem can be expressed as:

$$\sigma_e=\left[\sigma_{11}^2-\left(1+\frac{1}{S_2^2}-\frac{1}{S_3^2}\right)\sigma_{11}\sigma_{22}+\frac{1}{S_2^2}\sigma_{22}^2+\frac{3}{S_{12}^2}\sigma_{12}^2\right]^{1/2}. \tag{18}$$

For this material, the anisotropy variables S_{ij} were determined in Chen et al. (2018) using the tension–torsion experiments of Scales et al. (2019), and take the values

$$S_2=1.01,\quad S_3=0.97,\quad S_{12}=0.93$$

The corresponding material hardening response was extracted from the same pure torsion test used to extract the hardening responses for vM, H8 and Yld04-3D models adopted in the present study. An essential aspect of this extraction is the use of (18) and accounting for material frame rotation as described in Chen et al. (2018, 2019). The resultant hardening response is included in Fig. 1 where it is seen to be significantly different from that of the isotropic case (vM). It also differs from the response of the anisotropic Yld04-3D.

The calibrated H-48 yield function was used in (13) together with the corresponding material hardening response to estimate the plastic equivalent strain at the limit load for the same range of stress ratios, and the results are included in Fig. 6. Here again the material frame rotation was accounted for using the procedure outlined in Section 2.3. The H-48 predictions, although better than the vM results, remain significantly lower than the Yld04-3D strains for stress ratios smaller than about 1.5. This demonstrates again that quadratic yield functions, even one that accounts for anisotropy, are not appropriate for Al-alloys.

Before leaving this section, it is worth pointing out that the geometry of the test section used in the tension–torsion experiments of Scales et al. (2019) was designed to preclude buckling due to torsion. The experiments confirmed that the specimens did not buckle for the lowest value of $\alpha = 0.5$, which undergoes significant shear strain before reaching the limit load. It is thus important to emphasize that, for different geometries buckling may precede the limit load calculated through expressions (13).

4. Uniform thickness thin-walled tube under combined tension and torsion

The test section of the tension–torsion experiments of Scales et al. (2019) has a significant stabilizing effect on the structure. To demonstrate this effect on the limit load we also formulate the Considère limit load criterion for a long circular tube with uniform thickness loaded under radial nominal stress paths, $\Sigma = \alpha \mathcal{T}$. Here, in the absence of the circumferential constraint imposed by the geometry,

$$\sigma_{11} = 0. \tag{19a}$$

$$\text{Consequently, } dF = 0 \;\Rightarrow\; d\sigma_{22} = \sigma_{22} d\varepsilon_{22}, \tag{19b}$$

$$\text{and } dT = 0 \;\Rightarrow\; d\sigma_{12} = \sigma_{12}(d\varepsilon_{22} - d\varepsilon_{11}) \tag{19c}$$

$$\text{Then } d\sigma_e = \left[\frac{\partial \Phi}{\partial \sigma_{22}} + \frac{\sigma_{12}}{\sigma_{22}}\left(1 - \frac{d\varepsilon_{11}}{d\varepsilon_{22}}\right)\frac{\partial \Phi}{\partial \sigma_{12}} + \frac{\partial \Phi}{\partial \psi}\frac{d\psi}{d\sigma_{22}}\right]\sigma_{22} d\varepsilon_{22}, \tag{20a}$$

$$\text{and } d\varepsilon_e = \sigma_{22} d\varepsilon_{22}\left(1 + \frac{2\sigma_{12}}{\sigma_{22}}\frac{d\varepsilon_{12}}{d\varepsilon_{22}}\right)/\sigma_e. \tag{20b}$$

Using (20a) and (20b)

$$\frac{d\sigma_e}{d\varepsilon_e} = \sigma_e\left[\frac{\partial \Phi}{\partial \sigma_{22}} - \left(\frac{\frac{\sigma_{12}}{\sigma_{22}}\frac{\partial \Phi}{\partial \sigma_{11}}\frac{\partial \Phi}{\partial \sigma_{12}} + \frac{1}{2\sigma_{22}}\frac{\partial \Phi}{\partial \psi}\frac{\partial \Phi}{\partial \sigma_{12}}}{\frac{\partial \Phi}{\partial \sigma_{22}} + \frac{\sigma_{12}}{\sigma_{22}}\frac{\partial \Phi}{\partial \sigma_{12}}}\right)\right]. \tag{21}$$

For isotropic yield functions, $\frac{\partial \Phi}{\partial \psi} = 0$ and $\frac{\partial \Phi}{\partial \sigma_{11}} = -\frac{1}{2}\frac{\partial \Phi}{\partial \sigma_{22}}$, and so (21) becomes

$$\frac{d\sigma_e}{d\varepsilon_e} = \sigma_e \frac{\partial \Phi}{\partial \sigma_{22}}\left[1 + \frac{\frac{\sigma_{12}}{2\sigma_{22}}\frac{\partial \Phi}{\partial \sigma_{12}}}{\frac{\partial \Phi}{\partial \sigma_{22}} + \frac{\sigma_{12}}{\sigma_{22}}\frac{\partial \Phi}{\partial \sigma_{12}}}\right]. \tag{22}$$

For cases in which the limit load occurs at small values of ε_{11}, $\sigma_{22} \approx \alpha\sigma_{12}$ and (22) simplifies to

$$\frac{d\sigma_e}{d\varepsilon_e} = \sigma_e \frac{\partial \Phi}{\partial \sigma_{22}}\left[1 + \frac{\frac{1}{2\alpha}\frac{\partial \Phi}{\partial \sigma_{12}}}{\frac{\partial \Phi}{\partial \sigma_{22}} + \frac{1}{\alpha}\frac{\partial \Phi}{\partial \sigma_{12}}}\right]. \tag{23}$$

Specializing (23) to the von Mises yield function results in

$$\frac{d\sigma_e}{d\varepsilon_e} = \sigma_e \frac{(1 + 9/2\alpha^2)}{(1 + 3/\alpha^2)^{3/2}}. \tag{24}$$

(This differs to some degree from Hillier's (1963) Eq. (26) derived for a thin-walled plate under combined in-plane loads specialized to tension and shear, because of differences in the way the proportional loading is applied.) Applying Hosford(8) to (23) is algebraically more lengthy, so the critical state can be determined using the derivatives of Φ derived in Appendix C.

4.1. Limit load solution

In this case in general

$$\frac{\sigma_{22}}{\sigma_{12}} = \alpha e^{\varepsilon_{11}} \equiv \kappa(\varepsilon_{11}) \text{ and } \Phi = \Phi(\kappa, \psi) \tag{25}$$

Before proceeding to the Considère expression (22), the relationship between κ and ψ must be established for chosen values of α. From Appendix A $d\varepsilon_{12} = -d\psi$ holds also for this case, thus

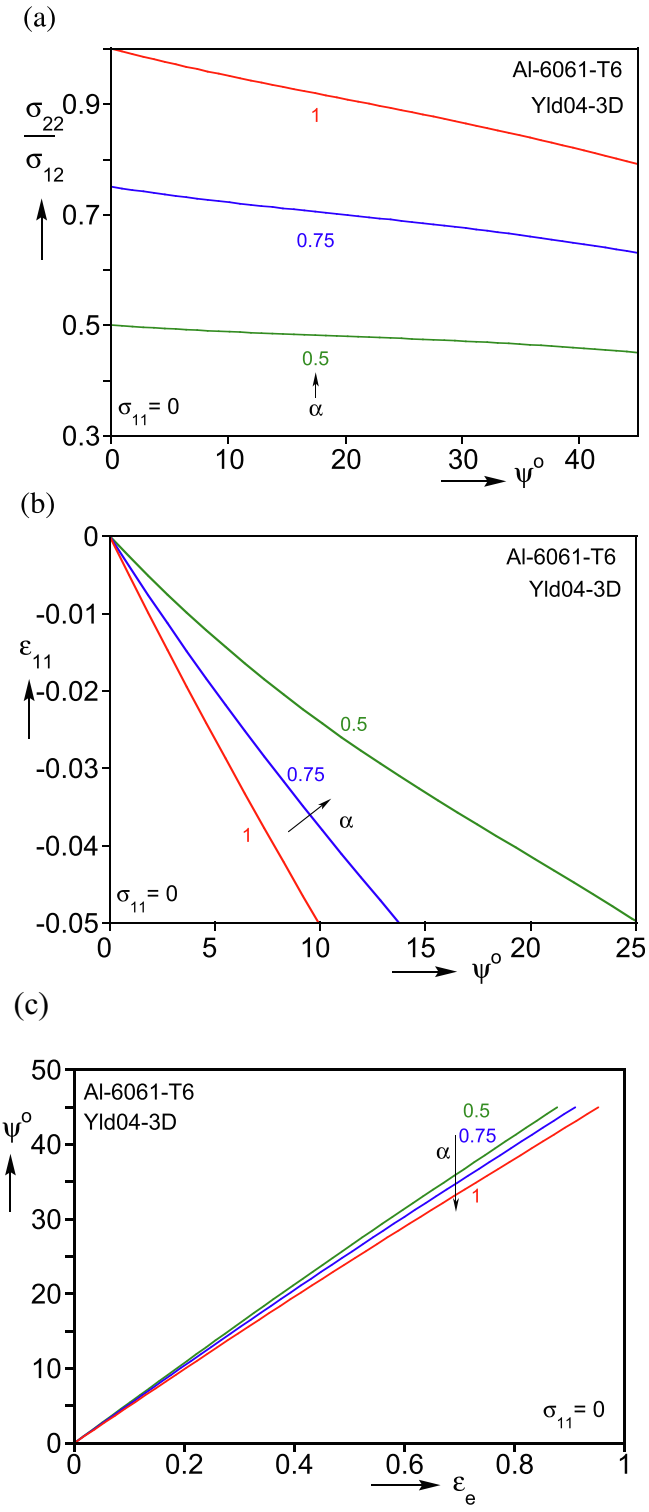

Fig. 8. (a) Stress ratio σ_{22}/σ_{12} vs. the material rotation angle ψ for three values of α for the uniform thickness tube ($\sigma_{11} = 0$). (b) Hoop strain vs. ψ, and (c) equivalent strain vs. ψ for the same values of α.

$$d\varepsilon_{11} = -2\left(\frac{\partial \Phi/\partial \sigma_{11}}{\partial \Phi/\partial \sigma_{12}}\right)d\psi \tag{26a}$$

Use (26a) in the difference scheme below to incrementally evaluate the stress ratio κ for different increments $d\psi$,

$$\kappa_{i+1} = \alpha \exp\left[\varepsilon_{11i} - 2\left(\frac{\partial \Phi/\partial \sigma_{11}}{\partial \Phi/\partial \sigma_{12}}\right)_{i+i} d\psi\right] \tag{26b}$$

Fig. 8a shows stress ratio - ψ relationships generated in this manner for three values of α; the difference from the nominal value is seen to increase as the material rotation angle increases. Fig. 8b plots ε_{11} against ψ for the same three nominal stress ratios.

The incremental relationship for the equivalent strain (20b) can be written as

$$d\varepsilon_e = -\frac{2\sigma_{22}}{\sigma_e}\left(\frac{\partial\Phi/\partial\sigma_{22}}{\partial\Phi/\partial\sigma_{12}} + \frac{\sigma_{12}}{\sigma_{22}}\right)d\psi \tag{27}$$

Since $\sigma_{22}/\sigma_e = f(\varepsilon_{11}, \kappa, \psi)$, use the $\psi - \kappa$ relationship for a chosen value of α to make the RHS of (27) strictly a function of ψ. Integration of (27) then produces relationships like those in Fig. 8c.

The critical state can then be evaluated form the Considère expression (22), as follows: Select a value of ε_e from the material hardening response and evaluate the corresponding σ_e and the local $d\sigma_e/d\varepsilon_e$. Obtain the corresponding frame rotation angle from the $\varepsilon_e - \psi$ relationship. Evaluate the derivatives of Φ using the corresponding values of κ and ψ, and compare the RHS of (22) with the value on the LHS. If they do not agree, increase ε_e and repeat until they do, which produces the critical state.

4.2. Results

The Considère expression (22) and the procedure outlined in Section 4.1 are now used to evaluate the equivalent plastic strain corresponding to the limit load, ε_{eL}, for different stress ratios, α. The strains are plotted in Fig. 9 against $\tan^{-1}\alpha$ for better clarity. Included are results for the vM, H8 and Yld04-3D yield functions, each used in conjunction with the corresponding material hardening response in Fig. 1. The Yld04-3D strains are higher than those of the other two yield functions with the difference progressively increasing from $\alpha \leqslant 1.0$. In this case H8 and vM produce essentially parallel trajectories with the one of vM being slightly higher, a trend that differs significantly from that of the circumferentially constrained case in Fig. 6. What is striking, however, is that the limit stains for this uniform geometry tube are significantly lower than those of the constrained geometry in Fig. 6. Thus, although the sharply increasing relationship between ε_{eL} and lower values of α is maintained, the Yld04-3D limit strain for the constrained case for $\alpha = 0.5$ are higher by a factor of about 1.92 but for $\alpha = 4$ they differ by only about 2%. This demonstrates the stabilizing role of the constrained geometry adopted in the experiments of Scales et al. (2019). The trend for vM is similar whereas for H8 the difference between the two geometries is much more pronounced. It is also important to point out that for lower values of α, bifurcation buckling in the form of a two-lobe ($n = 2$) spiral buckling mode can precede the limit load instability discussed in this section, rendering it impractical. This issue becomes even more severe for higher R/t_o tubes than the one used in this study.

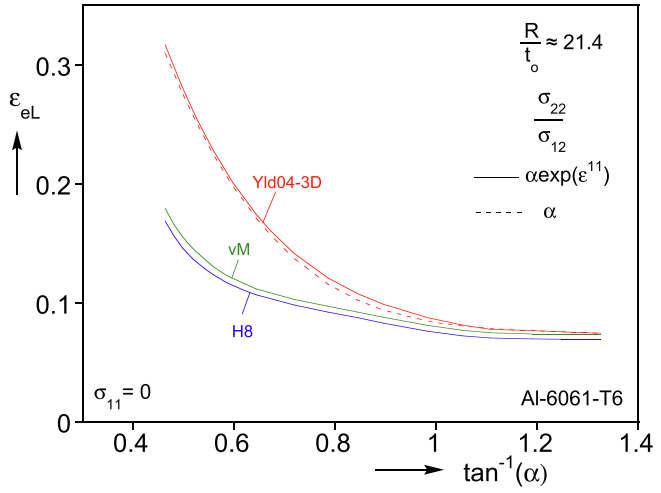

Fig. 9. Predicted equivalent strains at the limit loads vs. the stress ratio α for the uniform thickness tube. Included are predictions for Yld04-3D, vM and H8 constitutive models.

Fig. 9 includes with a dashed line the Yld04-3D limit strains predicted for $\sigma_{22}/\sigma_{12} \approx \alpha$, which of course simplifies the solution. Interestingly, for this material and geometry, the difference from the more exact solution is quite small for the whole range of stress ratios considered. The main cause for this close relationship is that the hoop strains ε_{11} produced at the limit load are rather small for the stress ratios considered. The difference between the more exact and approximate stress ratios for vM and H8 is similarly small and the results are not included.

5. Summary and conclusions

Under tensile loads thin-walled structures develop load maxima, or limit loads, beyond which deformation localizes leading to rupture. Thus, limit loads constitute forming limits for the structures. For structures such as sheet metal and tubes under uniform stresses, Considère-type estimates of limit loads provide simpler analytical alternatives to numerical calculations. This paper developed such estimates for anisotropic Al-alloy thin-walled tubes under combined tension and torsion. The anisotropy is modeled using the Yld04-3D with an exponent of 8 suitably calibrated, together with the material hardening response extracted from a simple shear test using this yield function. Shearing causes rotation of the material axes, and is accounted for in the process. Material frame rotation affects also the equivalent stress and strain on which Considère calculations are based. The present study describes how to analytically account for material frame rotation in limit load estimates for thin-walled tubes under combined tension and torsion. The analysis is verified by comparisons of the calculated strains at the limit loads with those measured in the circumferentially constrained tension–torsion experiments of Scales et al. (2019), and by FE simulations. Following are observations, comments, and conclusions drawn from this study.

a. The adoption of a non-quadratic anisotropic yield function in limit load calculations is essential for Al-alloys. Furthermore, the material hardening response extracted from a uniaxial or pure/simple shear test must be extracted using the same anisotropic yield function.
b. In the present study the material hardening came from a simple shear test. Deformation induced by simple shear results in rotation of the material frame and this must be accounted for.
c. The combined shear-tension state of stress of the tension–torsion experiments of Scales et al. (2019) leads to a limit load, which can be predicted by Considère-type analysis. This biaxial state of stress results in material frame rotation, which must also be accounted for in the calculation of the equivalent stress and strain.
d. Considère-type calculations reproduced accurately the measured limit loads by: (i) adopting the Yld04-3D yield function; (ii) using a material hardening response extracted as in point b; and (iii) accounting for material frame rotation in the calculation of the equivalent stress and strain. By contrast, calculations based on vM, H8 and H-48 deviate from the measured results increasingly so as the stress ratio decreases.

e. The tension–torsion experiments simulated were performed under radial nominal stress paths $\Sigma = \alpha\mathcal{T}$. The corresponding true stresses are $\sigma_{22} = \alpha\sigma_{12}e^{\varepsilon_{11}}$ and this difference can affect the analytical calculation of the limit state.
f. The circumferential constraint of the experimental setup of Scales et al. (2019) has a strong stabilizing effect on the structure. Thus, the strains corresponding to the limit loads for a uniform tube tested under the same radial stress paths are significantly smaller for shear-dominant stress states. It is also important to point out that in the case of the uniform tube with lower values of α, bifurcation buckling in the form of a spiral buckling mode can precede the limit load instability predicted. Buckling becomes more likely as R/t_o increases.

Declaration of Competing Interest

The authors declare that they have no known competing financial interests or personal relationships that could have appeared to influence the work reported in this paper.

Acknowledgments

The authors acknowledge with thanks financial support received for this work from the National Science Foundation through the GOALI grant CMMI-1663269. Thanks are also due to Martin Scales for help in the extraction of results from the tension-torsion experiments.

Appendix A Material frame rotation

Case I: $\varepsilon_{11} = 0$

Consider a material element in the 1-2 frame that is undergoing shear and stretch as shown in Fig. A1.The deformation gradient, $\boldsymbol{F}$, is

$$\boldsymbol{F} = \begin{bmatrix} 1 & \gamma & 0 \\ 0 & \lambda & 0 \\ 0 & 0 & 1/\lambda \end{bmatrix}. \tag{A1}$$

where λ is the axial stretch and γ is the normalized shear displacement. The incremental strain is

$$d\boldsymbol{\varepsilon} = sym(\boldsymbol{dF}\cdot\boldsymbol{F}^{-1}) = \begin{bmatrix} 0 & d\gamma/2\lambda & 0 \\ d\gamma/2\lambda & d\lambda/\lambda & 0 \\ 0 & 0 & -d\lambda/\lambda \end{bmatrix}, \tag{A2a}$$

and the instantaneous spin tensor is

$$d\boldsymbol{\omega} = skewsym(\boldsymbol{dFF}^{-1}) = \begin{bmatrix} 0 & d\gamma/2\lambda & 0 \\ -d\gamma/2\lambda & 0 & 0 \\ 0 & 0 & 0 \end{bmatrix}. \tag{A2b}$$

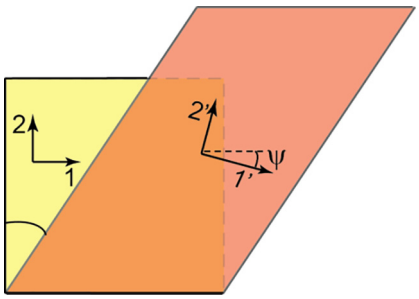

Fig. A1. Sheared and stretched material element for $\varepsilon_{11} = 0$; shown are the initial and rotated material axes.

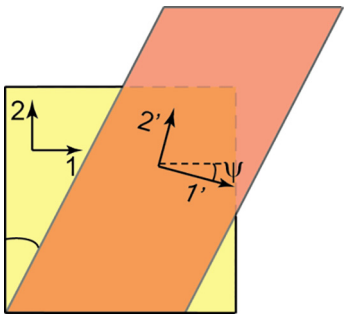

Fig. A2. Sheared and stretched material element for $\sigma_{11} = 0$.

The instantaneous material frame rotation depicted in Fig. A1 is

$$d\psi = -d\gamma/2\lambda = -d\varepsilon_{12} \tag{A3}$$

It is worth pointing out that $d\boldsymbol{\omega}$ corresponds to the incremental form of the rotation tensor of polar decomposition, which we consider more appropriate for incremental plasticity applications such as the present one. It is also consistent with how frame rotation is handled in ABAQUS (2016) that was employed to calculate the response using the finite element model.

Case II: $\sigma_{11} = 0$

In this case $\lambda_1 \neq 0$ and because of the material anisotropy $\lambda_3 \neq \lambda_1$. The deformed material element now becomes:

$$\text{Then } \boldsymbol{F} = \begin{bmatrix} \lambda_1 & \gamma & 0 \\ 0 & \lambda & 0 \\ 0 & 0 & \lambda_3 \end{bmatrix}, \quad \lambda_3 = \frac{1}{\lambda\lambda_1}. \tag{A4}$$

Furthermore $d\boldsymbol{\varepsilon} = sym(\boldsymbol{dF}\cdot\boldsymbol{F}^{-1})$

$$= \begin{bmatrix} d\lambda_1/\lambda_1 & (d\gamma/2\lambda - \gamma d\lambda_1/2\lambda\lambda_1) & 0 \\ (d\gamma/2\lambda - \gamma d\lambda_1/2\lambda\lambda_1) & d\lambda/\lambda & 0 \\ 0 & 0 & d\lambda_3/\lambda_3 \end{bmatrix}, \tag{A5a}$$

and $d\boldsymbol{\omega} = skewsym(d\boldsymbol{FF}^{-1})$

$$= \begin{bmatrix} 0 & (d\gamma/2\lambda - \gamma d\lambda_1/2\lambda\lambda_1) & 0 \\ -(d\gamma/2\lambda - \gamma d\lambda_1/2\lambda\lambda_1) & 0 & 0 \\ 0 & 0 & 0 \end{bmatrix}. \tag{A5b}$$

$$\text{Thus } d\psi = -(d\gamma/2\lambda - \gamma d\lambda_1/2\lambda\lambda_1) = -d\varepsilon_{12}. \tag{A6}$$

Appendix B Hosford (8) for $\varepsilon_{11} = 0$

For this yield function the value of the stress ratio $\sigma_{11}/\sigma_{22} = \beta$ depends on the applied stress proportionality constant α. β can be related to α through the hoop strain constraint $d\varepsilon_{11} = 0$which implies that

$$\frac{\partial\Phi}{\partial\sigma_{11}} = 0 = \frac{\partial\Phi}{\partial\sigma_1}\frac{\partial\sigma_1}{\partial\sigma_{11}} + \frac{\partial\Phi}{\partial\sigma_2}\frac{\partial\sigma_2}{\partial\sigma_{11}} \tag{B1}$$

The derivatives on the RHS of (B1) are:

$$\frac{\partial\Phi}{\partial\sigma_1} = \frac{1 + (1-\Gamma)^7}{2^{1/8}\left[1 + \Gamma^8 + (1-\Gamma)^8\right]^{7/8}}, \qquad \frac{\partial\Phi}{\partial\sigma_2} = \frac{\Gamma^7 - (1-\Gamma)^7}{2^{1/8}\left[1 + \Gamma^8 + (1-\Gamma)^8\right]^{7/8}}, \tag{B2a}$$

where $\Gamma = \sigma_2/\sigma_1$ is given in Eq. (17b), and

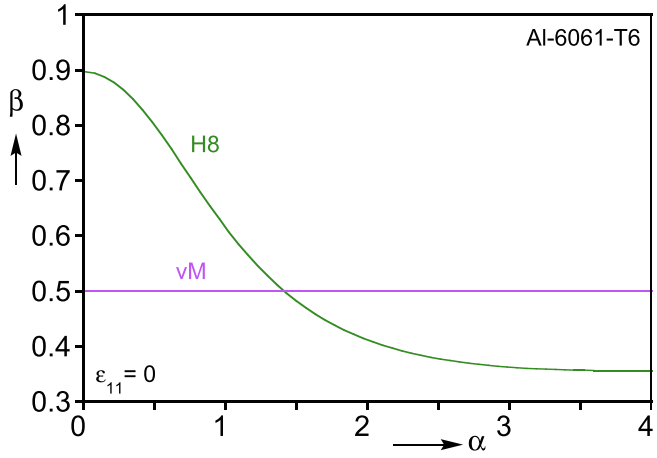

Fig. B1. Stress ratio $\beta = \sigma_{11}/\sigma_{22}$ vs. α for the Hosford(8) and von Mises yield functions.

$$\frac{\partial\sigma_{1,2}}{\partial\sigma_{11}} = \frac{1}{2}\left\{1 \pm \frac{(1-\beta)}{[(\beta-1)^2 + 4/\alpha^2]^{1/2}}\right\}. \tag{B2b}$$

Thus (B1) can be written as:

$$(1+\Gamma^7)[(1-\beta)^2 + 4/\alpha^2]^{1/2} - [2(1-\Gamma)^7 + 1 - \Gamma^7](1-\beta) = 0. \tag{B3}$$

Solving (B3) for specific values of α produces the relationship plotted in Fig. B1.

Appendix C Hosford (8) for $\sigma_{11} = 0$

For a uniform thickness tube under combined tension and torsion, the principal stresses can be written as:

$$\Gamma_{1,2} = \frac{\sigma_{22}}{2}\left[1 \pm \sqrt{1 + 4/\alpha^2}\right]$$
$$\text{and } \Gamma = \frac{\sigma_2}{\sigma_1} = \frac{1 - [(1+4/\alpha^2]^{1/2}}{1 + [(1+4/\alpha^2]^{1/2}}. \tag{C1}$$

$$\text{Then } \frac{\partial\sigma_{1,2}}{\partial\sigma_{22}} = \frac{1}{2}\left\{1 \pm \frac{1}{[1+4/\alpha^2]^{1/2}}\right\} \text{ and}$$
$$\frac{\partial\sigma_{1,2}}{\partial\sigma_{12}} = \pm\frac{1}{[1+4/\alpha^2]^{1/2}}. \tag{C2}$$

Thus, the derivatives of Φ on the RHS of (23) can be expressed as

$$\frac{\partial\Phi}{\partial\sigma_{22}} = \frac{1 + \Gamma^7 + [1 - \Gamma^7 + 2(1-\Gamma)^7]/[1 + 4/\alpha^2]^{1/2}}{2^{9/8}[1 + \Gamma^8 + (1-\Gamma)^8]^{7/8}}, \tag{C3}$$

$$\text{and } \frac{\partial\Phi}{\partial\sigma_{12}} = \frac{[1 - \Gamma^7 + 2(1-\Gamma)^7]}{2^{1/8}[1 + \Gamma^8 + (1-\Gamma)^8]^{7/8}[1 + \alpha^2/4]^{1/2}}. \tag{C4}$$

References

ABAQUS, 2016, Theory Guide, Section 1.4.3, Dassault Systèmes Simulia Corp. Providence, RI, USA.

Abedini, A., Noder, J., Kohar, C.P., Butcher, C., 2020. Accounting for shear anisotropy and material frame rotation on the constitutive characterization of automotive alloys using simple shear tests. Mech. Mater. 148, 103419. https://doi.org/10.1016/j.mechmat.2020.103419.

Barlat, F., Aretz, H., Yoon, J.W., Karabin, M.E., Brem, J.C., Dick, R.E., 2005. Linear transformation-based anisotropic yield functions. Int. J. Plasticity 21, 1009–1039. https://doi.org/10.1016/j.ijplas.2004.06.004.

Butcher, C., Abedini, A., 2019. On phenomenological failure loci of metals under constant stress rates of combined tension and shear: Issues of coaxiality and non-uniqueness. Metals 9, 1052. https://doi.org/10.3390/met9101052.

Chen, K., Scales, M., Kyriakides, S., 2019. Material response, localization, and failure of an aluminum alloy under combined shear and tension: part II Analysis. Int. J. Plasticity 129, 361–379. https://doi.org/10.1016/j.ijplas.2019.04.002.

Chen, K., Scales, M., Kyriakides, S., 2018. Effect of material frame rotation on the hardening of an anisotropic material in simple shear tests. ASME. J. Appl. Mech. 85, 1–5. 12501. https://doi.org/10.1115/1.4041320.

Considère, A., 1885. Mémoire sur l'emploi du fer et de l'acier dans les constructions. Annales des Ponts et Chaussées, Série 6 (9), 574–575.

Hillier, M.J., 1963. Tensile plastic instability under complex stress. J. Mech. Eng. Sci. 5 (1), 57–67. https://doi.org/10.1016/0020-7403(63)90039-0.

Hillier, M.J., 1974. Necking of anisotropic plastic material. Int'l J. Solids Struct. 10, 211–215. https://doi.org/10.1016/0020-7683(74)90019-5.

Hill, R., 1948. A theory of the yielding and plastic flow of anisotropic metals. Proc. R Soc. Lond. A 193, 281–297. https://doi.org/10.1098/rspa.1948.0045.

Hill, R., 1996. A general theory of plastic deformation and instability in thin-walled tubes under combined loading. J. Mech. Phys. Solids 44 (12), 2041–2057. https://doi.org/10.1016/S0022-5096(96)00062-2.

Hosford, W.F., 1972. A generalized isotropic yield criterion. ASME J. Appl. Mech. 39, 607–609. https://doi.org/10.1115/1.3422732.

Mellor, P.B., 1962. Tensile instability in thin-walled tubes. J. Mech. Eng. Sci. 4 (3), 251–256. https://doi.org/10.1243/JMES_JOUR_1962_004_034_02.

Scales, M., Chen, K., Kyriakides, S., 2019. Material response, localization, and failure of an aluminum alloy under combined shear and tension: Part I Experiments. Int'l J. Plasticity 129, 340–360. https://doi.org/10.1016/j.ijplas.2019.04.004.

Scales, M., Chen, K., Kyriakides, S., 2021. Response, localization and rupture of anisotropic tubes under combined pressure and tension. ASME J. Appl. Mech. 88 (011008), 1–11. https://doi.org/10.1115/1.4048648.

Stout, M.G., Hecker, S.S., 1983. Role of geometry in plastic instability and fracture of tubes and sheet. Mech. Mater. 2 (1), 23–31. https://doi.org/10.1016/0167-6636(83)90005-4.

Swift, H.W., 1952. Plastic instability under plane stress. J. Mech. Phys. Solids 1 (1), 1–18. https://doi.org/10.1016/0022-5096(52)90002-1.

Tardif, N., Kyriakides, S., 2012. Determination of anisotropy and material hardening for aluminum sheet metal. Int'l J. Solids Struct. 49 (25), 3496–3506. https://doi.org/10.1016/j.ijsolstr.2012.01.011.